Multiple-Incidence and Multifrequency for Profile Reconstruction of Random Rough Surfaces Using the 3-D Electromagnetic Fast Multipole Model

Magda El-Shenawee, *Senior Member, IEEE,* and Eric L. Miller, *Member, IEEE*

***Abstract*—A fast algorithm for reconstructing the profile of random rough surfaces using electromagnetic scattering data is presented. The algorithm is based on merging a fast forward solver and an efficient optimization technique. The steepest descent fast multipole method is used as the three-dimensional fast forward solver. A rapidly convergent descent method employing a "*marching-on*" strategy for processing multifrequency and multi-incidence angle data is introduced to minimize an underlying cost function. The cost function represents the error between true (synthetic) and simulated scattered field data. Several key issues that impact the accuracy in reconstructing the rough profile are examined in this work, e.g., the location and number of receivers, the incident and scattered directions, the surface roughness, and details regarding the manner in which sensitivity information is computed in the inversion scheme. The results show that using the multiple-incidence (*one angle at a time*) and the multifrequency (*one frequency at a time*) strategies lead to improve the profile reconstruction.**

***Index Terms*—Fast algorithms, inverse scattering, optimization techniques, profile reconstruction, rough surface scattering.**

I. Introduction

THE PRESENCE of rough ground surface is considered a major source of clutter in subsurface sensing applications. The ground roughness causes considerable distortion to ground-penetrating radar response (GPR), which makes it difficult for conventional signal processing techniques to be of use in processing the received GPR data. In some cases, it could be life threatening to experimentally measure the roughness of the ground profile (e.g., landmine fields). This is a significant challenge for subsurface sensing researchers. Therefore, the motivation of this work is to predict the random rough profile of the ground using a fast inversion algorithm.

This paper is related to two broad topics currently addressed in the literature: 1) forward scattering of electromagnetic fields from rough surfaces without or with buried targets [1]–[24] and 2) estimating the surface profile or roughness statistics based on theoretical, experimental, or computational techniques [25]–[38]. Several works have been published to analyze the electromagnetic field scattered from one-dimensional (1-D) and two-dimensional (2-D) random rough surfaces without and with buried targets [1]–[24], respectively. However, less has appeared on reconstructing the profile of rough surfaces especially the 2-D random rough dielectric surfaces [25]–[38]. The work in [25] and [26] presents methods for inferring roughness parameters of 1-D surfaces from the average electromagnetic data. The work in [27] and [28] discusses some analytical and experimental methods to determine the roughness statistics of 1-D and 2-D surface profiles using electromagnetic data. All work in [29]–[37] present methods for reconstructing the profile of 1-D rough surfaces, either perfect electric conducting (PEC) surfaces [29]–[33] or dielectric surfaces [34]–[37]. The work in [38] presents a technique for 2-D PEC rough profile reconstruction. In reality, the ground is randomly rough in two dimensions (i.e., x and y directions) with nonperfect conducting material (e.g., soil, sand, vegetation, water, etc.), which makes it more challenging to reconstruct its profile.

Our algorithm is based on combining a three-dimensional (3-D) fast forward solver with nonlinear programming technique, which uses electromagnetic waves scattered from the rough ground surface (GPR-type data). The well-developed steepest descent fast multipole method (SDFMM) will be used here as the fast forward solver [14]–[19], [39]–[41]. Briefly, the SDFMM is a hybridization of the fast multipole method (FMM) [39]–[41], the method of moments (MoM) [42], [43], and the steepest descent (SD) integration rule [41]. This fast forward solver is combined with the efficient optimization technique of Fletcher and Powell [44]–[46] to minimize a cost function relating parameters of the unknown surface structure to the observed field data. Although real collected GPR data should be used in the reconstruction process, for simplicity in this paper, synthetic data, generated using the 3-D SDFMM computer code, will be used to test the reconstruction algorithm. Several key issues will be examined such as the reconstruction accuracy, the influence of number and locations of receivers, the computational expenses of the algorithm, the type of cost function (e.g., complex or amplitude error of electric field), and the surface roughness.

It is important to emphasize that the concept of combining a forward scattering solver with an optimization technique is similar to the concept used in [34]–[38]. This paper is based on an integral-equation-FMM computational technique that accounts for all multiple-scattering mechanisms from the surface; however, the work in [34]–[38] was based on Kirchhoff approximation, which accounts only for the single scatter and not the multiple scattering [13].

Manuscript received February 20, 2004; revised July 6, 2004. This work was supported in part by the National Science Foundation (NSF) Center for Subsurface Sensing and Imaging Systems (CenSSIS) at Northeastern University under Award EEC-9986821 and in part by the NSF under Awards 0208548 and 0139968.

M. El-Shenawee is with the Department of Electrical Engineering, University of Arkansas, Fayetteville AR 72701 USA (e-mail: magda@uark.edu).

E. L. Miller is with the Center for Subsurface Sensing and Imaging Systems, Department of Electrical and Computer Engineering, Northeastern University, Boston, MA 02115 USA (e-mail: elmiller@ece.neu.edu).

Digital Object Identifier 10.1109/TGRS.2004.834762

Our inversion technique uses *marching-on* schemes of the incident angle and frequency. One issue that often arises with *marching-on* methods, is how to choose the criteria for deciding the order and length of each scheme. In this paper, we present results indicating that *marching-on* methods offer a feasible approach to provide high-quality reconstruction of rough surfaces. We consider, beyond the scope of this paper, the more general questions concerning synthesizing specific iterative strategies for nonlinear problems to guarantee some level of convergence (e.g., data ordering, number of iterations per data subset, etc.). Such problems are difficult as generally discussed, but not dealt with, by Natterer and Wubbeling [47] and Dorn *et al.* [48]. The application-oriented work presented here is an attempt to answer some of these questions.

This paper is organized as follows. The methodology of the algorithm and mathematical formulations are summarized in Section II and in Appendix A and B. The numerical results are presented and discussed in Section III, and the concluding remarks are given in Section IV.

II. Methodology

The reconstruction algorithm of the rough surface profile begins with assuming a mathematical model of the surface that can approximately define its height variation. This surface model includes a number of unknown parameters that need to be recovered during the reconstruction process. For example, the surface profile can be assumed deterministic (e.g., sinusoidal), similar to the work reported in [38], or random based on the B-spline function, similar to the work reported in [34]–[37]. The second key issue of the algorithm is to define an appropriate cost function to be minimized. This cost function represents the error between true data (GPR-type data) and simulated data generated during the searching process. The third key issue is computing the synthetic and simulated data using the direct method based on a 3-D fast forward solver of the electromagnetic waves. In this paper, we examine the utility of two cost functions $C(\theta)$ defined as

$$C_1(\theta)=\sum_{i=1}^{N_r}\left|\left|\overline{E}_i^{\text{True}}\right|-\left|\overline{E}_i^{\text{Sim}}(\theta)\right|\right|^2$$
$$C_2(\theta)=\sum_{i=1}^{N_r}\left|\overline{E}_i^{\text{True}}-\overline{E}_i^{\text{Sim}}(\theta)\right|^2 \tag{1}$$

in which $\overline{E}_i^{\text{True}}$ and $\overline{E}_i^{\text{Sim}}$ represent the scattered complex electric fields for true data (GPR-type data) and simulated data, respectively. The subscript i represents the receiver's number, where N_r is the total number of receivers located above the ground. The vector θ represents the unknown parameters to be recovered in order to reconstruct the profile of the rough surface. The number of elements of vector θ varies according to the assumed mathematical model of the surface profile. For example, θ includes two parameters in case of sinusoidal surfaces, but it could include more parameters in case of using B-spline functions, as will be discussed in Section III. The cost function in (1) will be minimized until an acceptable error is achieved as discussed later in this section.

A. Forward Scattering (Direct) Method

All field computations, either to generate synthetic data $\overline{E}_i^{\text{True}}$ or simulated fields $\overline{E}_i^{\text{Sim}}$ at each receiver, are obtained using the 3-D SDFMM fast forward solver [41]. The SDFMM accelerates the MoM solution of the surface integral equations given by [41]–[43]

$$\overline{E}^{\text{inc}}(\overline{r})\Big|_{\text{tang.}}=\left[(L_1+L_2)\,\overline{J}-(K_1+K_2)\,\overline{M}\right]_{\text{tang.}} \tag{2a}$$
$$\overline{H}^{\text{inc}}(\overline{r})\Big|_{\text{tang.}}=\left[(K_1+K_2)\,\overline{J}+\left(\frac{L_1}{\eta_1^2}+\frac{L_2}{\eta_2^2}\right)\overline{M}\right]_{\text{tang.}} \tag{2b}$$

where tang. refers to tangent to the scatterer's surface S_1, $\overline{J}$ and $\overline{M}$ are the surface electric and magnetic currents, respectively, $\overline{r}$ is the position vector, and η_1 and η_2 are the intrinsic impedances of the air and the ground, respectively. The expressions of the integro-differential operators $L_{1,2}$ and $K_{1,2}$ are given in Appendix A. Upon discretizing the surface S_1 using the Raw–Wilton–Glisson (RWG) triangular patches, the surface currents, $\overline{J}$ and $\overline{M}$, are approximated by [41]–[43]

$$\overline{J}(\overline{r})=\sum_{n=1}^{N}I_{1n}\overline{j}_n(\overline{r})\quad \overline{M}(\overline{r})=\eta_1\sum_{n=1}^{N}I_{2n}\overline{j}_n(\overline{r}),\qquad \overline{r}\in S_1 \tag{3}$$

in which $\overline{j}$ is a vector basis function, and $I=[\,I_1\quad I_2\,]$ is the current unknown coefficient vector. After some algebraic manipulations, a linear system of equations is obtained, $\overline{\overline{Z}}\overline{I}=\overline{V}$. The expression of the impedance matrix $\overline{\overline{Z}}$ is given in Appendix A, and the vector $\overline{V}$ is the tested tangential incident electric field $\overline{E}^{\text{inc}}$ and normalized magnetic field $\eta_1\overline{H}^{\text{inc}}$ on the scatterer's surface S_1 [41]–[43]. As is well known, using the MoM to solve this system of equations is computationally expensive either for large-scale scatterers or when the scatterer is involved in inversion techniques. Therefore, the fast forward solver (the SDFMM) is employed in the current inversion algorithm. Basically, when using the FMM [39]–[41], the matrix $\overline{\overline{Z}}$ is expressed as $\overline{\overline{Z}}^{\text{NF}}+\overline{\overline{Z}}^{\text{FF}}$, where $\overline{\overline{Z}}^{\text{NF}}$ and $\overline{\overline{Z}}^{\text{FF}}$ represent the near field (NF) and the far field (FF) parts, respectively [39]–[41]. The elements of $\overline{\overline{Z}}^{\text{NF}}$ are computed directly and are multiplied by the vector $\overline{I}$ similar to the standard MoM, while the elements of $\overline{\overline{Z}}^{\text{FF}}$ are not directly computed nor stored, but their contribution to the matrix vector multiplication is conducted in one step using the inhomogeneous plane wave expansions [39]–[41]. The interaction decomposition into near field (NF) and far field (FF) is implemented according to the distance, in free-space wavelength, between the interacting elements on the scatterer's surface [39]–[41]. As reported by Jandhyala [41], the computational complexity of the SDFMM is $O(K)$, for the CPU time and computer memory requirements per iteration, while it is $O(K^2)$ for the MoM, where K is the total number of surface current unknown coefficients. Once the surface currents are computed, the scattered (radiated) electric fields $\overline{E}_i^{\text{Sim}}$ can be easily obtained in both the near and/or the far zone, similar to the work reported in [14]–[19].

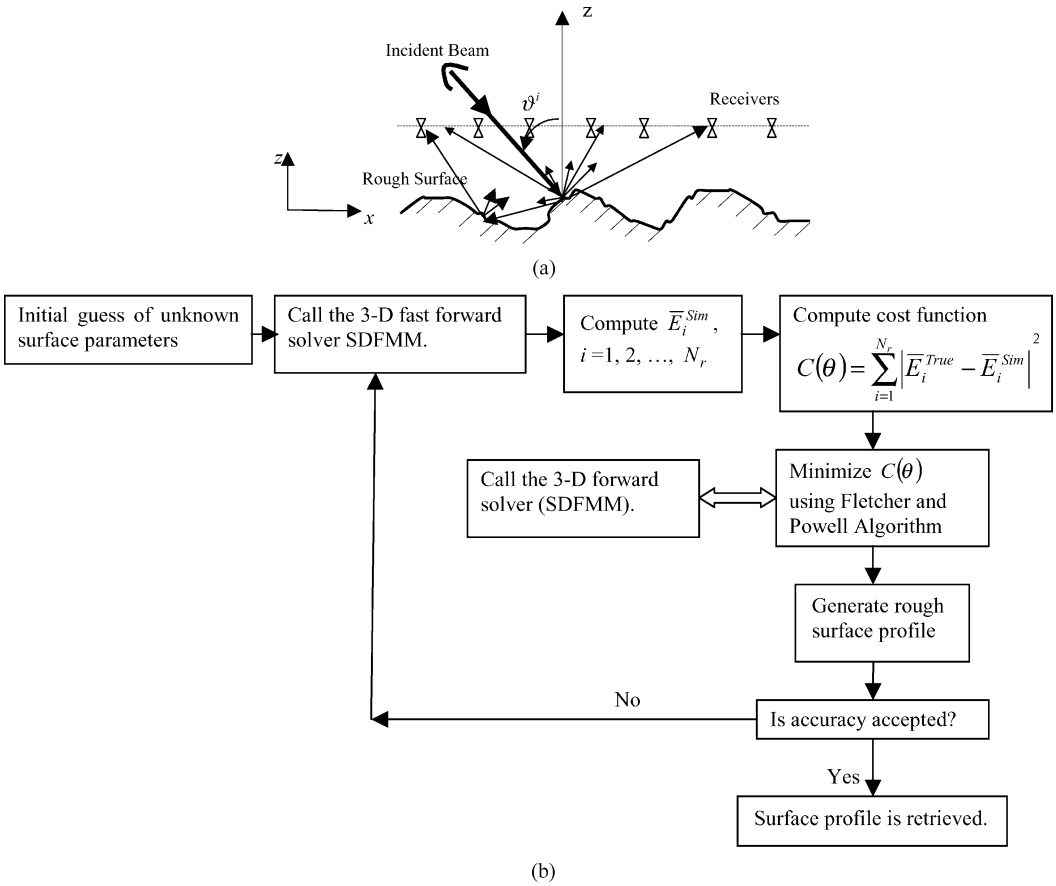

Fig. 1. (a) Problem configuration (cross section). (b) Flowchart of inversion algorithm.

B. Optimization Method

The estimated vector $\hat{\theta}$ will be obtained upon minimizing the cost function $C(\theta)$ in (1) as

$$\hat{\theta} = \arg_{\theta}(\min(C(\theta))). \tag{4}$$

A rapid steepest decent optimization approach, developed by Fletcher and Powell [44]–[46], is implemented here. For faster and more efficient computations, the elements of the unknown vector θ will be restricted to certain limits, i.e., upper and lower bound constraints will be *a priori* provided ($\theta_{\rm LB} \leq \theta \leq \theta_{\rm UB}$). In its most basic form (without the constraints), the iterative inversion technique to search for the unknown vector θ is given by [44]–[46]

$$\hat{\theta}_{k+1} = \hat{\theta}_k + \alpha_k d_k \tag{5a}$$

in which k is the iteration index, α_k is the k step, and the vector d_k is the vector that minimizes the quadratic equation $q(d)$ as (see details of Fletcher and Powell algorithm in [44]–[46])

$$q(d) = 0.5 d^T H_k d + c^T d, \qquad d \in R^n \tag{5b}$$

in which R is the real domain, $c = \nabla C\left(\hat{\theta}_k\right)$ is the gradient of the cost function $C(\theta)$, and the matrix H contains the true curvature information for the feasible region and can be regarded as a reduced inverse Hessian matrix (see [44]–[46] for details including a discussion concerning the manner in which bound constraints are incorporated into the processing).

Computationally, a key component of this approach is the calculation of the gradient of the cost function. In this paper, we make use of finite-difference approximations for the required sensitivity analysis [49]. Although such methods are somewhat less efficient than adjoint field techniques, they are more straightforward to code (especially given the SDFMM forward model) and provide the necessary proof-of-principle results for this paper. Indeed, the strong performance of the method obtained in this paper provides motivation for developing the required adjoint field computational tools based on the SDFMM forward model.

To be specific, the gradient of the cost function is evaluated numerically using the central or the forward difference equations [49]. Equation (5a) shows that solving the inverse problem requires solving the forward problem large number of times, either to compute $\overline{E}_i^{\rm Sim}$ at each receiver in (1) or to compute the gradient c in (5b) with respect to each parameter of vector θ. Notice that the mathematical model assumed for the unknown rough surface profile determines the number of associated parameters of θ. Consequently, it determines the number of derivatives involved in the gradient $c = \nabla C\left(\hat{\theta}_k\right)$. It is also important to emphasize that each iteration of the Fletcher and Powell search algorithm involves studying the behavior of the cost function in order to determine the best possible search direction (see details in [44]–[46]). This implies that for each iteration k, several runs of the 3-D forward solver are required. This scenario necessitates using an efficient and fast forward solver, such as the SDFMM, to retrieve the surface profile

in realistic time. The geometry of the problem is shown in Fig. 1(a), while the flowchart of the inversion algorithm is shown in Fig. 1(b).

When using a gradient descent method to solve nonlinear inverse problems, several important issues arise including: 1) the mathematical model of the unknown rough surface profile with its unknown parameters; 2) the behavior of cost functions with respect to variations in these parameters; and 3) the convergence of the algorithm with respect to the initial guess of these parameters. In addressing 1), we make use of a number of well-studied parametric models for the roughness profile. Unfortunately, issues 2) and 3) are less amenable to meaningful closed-form analysis. Thus, we present here a number of numerical examples that illustrate the general behavior of the cost function and convergence of the inversion method, which we see across the range of examples provided in Section III.

The results, for investigating the above issues, are obtained using the fast forward solver SDFMM for a surface size 1.224×1.224 m^2 at $f = 1$ GHz. The incident electromagnetic wave is represented by a Gaussian beam normally incident to the surface with horizontal polarization [2], [14]–[19]. The incident beam illuminates a circular spot on the ground of diameter ~ 49 cm. In this section, the relative dielectric constant of the ground is assumed $\varepsilon_r = 2.5 - i0.18$ (Bosnian dry soil [14]). The horizontal electric field scattered from the ground in the far zone at normal incidence is calculated to obtain the cost function $C(\theta)$. This implies that the copolarized waves (HH) are obtained at single receiver, i.e., $N_r = 1$, in this example. In all results presented in this paper, the interactions between elements on the scatterer's surface are considered FF when their FMM blocks are separated by two or more finest blocks, where each block has dimensions of $0.32\lambda_0 \times 0.32\lambda_0$ [41].

C. Rough Surface Models

To investigate the above issues, two rough surface models are used as follows.

1) Two-Dimensional Sinusoidal Rough Surface: In Example 1, the surface is assumed sinusoidal similar to Harada and Noguchi [38] ($h(x,y) = H\cos(2\pi x/L)\cos(2\pi y/L)$), where H and L are the surface maximum height and period, respectively. The behavior of the cost function $C_1(\theta)$ in (1) is plotted versus the surface parameters H and L as shown in Fig. 2(a). The results show a pronounced minimum point for $L = 1\lambda_0$ and $H = 0.15\lambda_0$. The inversion algorithm is tested to recover the unknown parameter H, assuming, for simplicity, that the surface period is known ($L = 1\lambda_0$), as shown in Fig. 2(b). Zero initial value of H (i.e., flat surface) is used in the algorithm recovering a sinusoidal surface with relative error less than 3% with respect to the true surface.

2) Two-Dimensional B-Spline Rough Surface: In Example 2, the previous test is repeated for a 2-D rough surface approximated by a tensor-product B-spline function as follows [34], [50], [51]:

$$h(x,y) \approx \sum_{n=-4}^{N_n-1} \sum_{m=-4}^{N_m-1} \alpha_{n,m} S_n(x) S_m(y) \tag{6a}$$

in which $\alpha_{n,m}$ are the unknown coefficients with total numbers of $N_n + 4$ and $N_m + 4$ in x and y directions, respectively, and

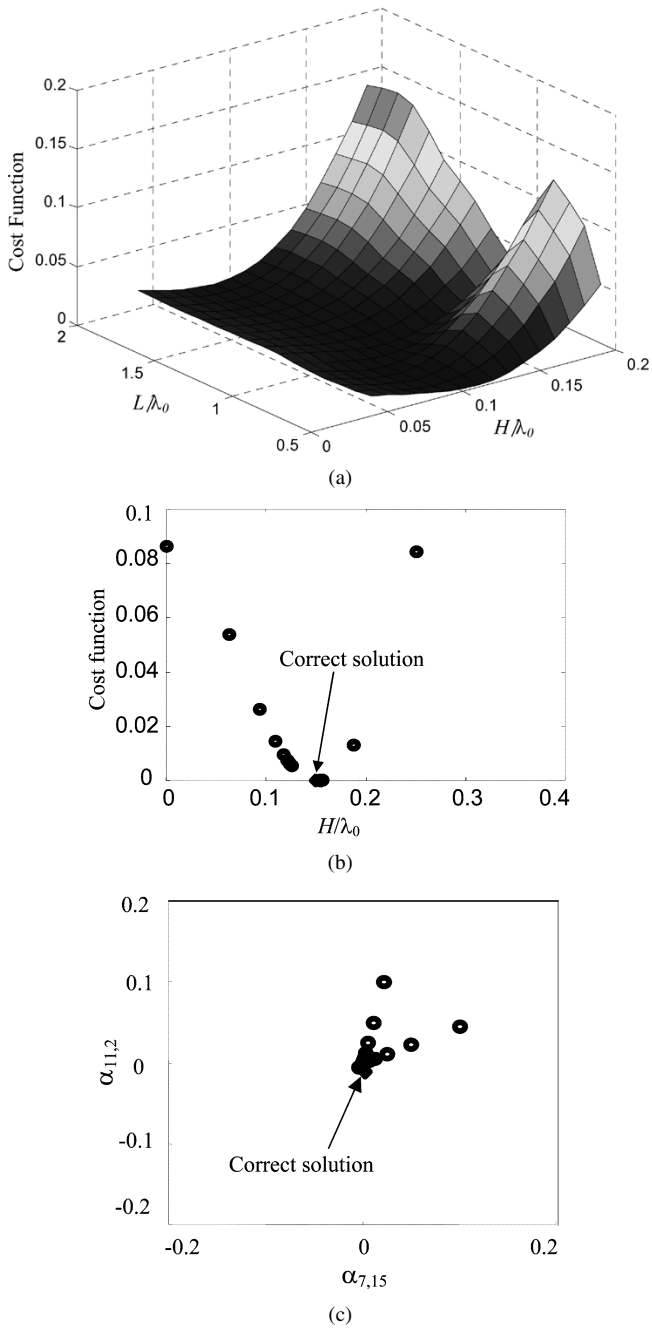

Fig. 2. (a) Cost function behavior for 2-D sinusoidal surface. (b) Convergence of inversion algorithm of 2-D sinusoidal surface, assuming a surface period of $L = 1\lambda_0$. (c) Convergence of inversion algorithm for 2-D tensor-product spline-function model with two unknown coefficients ($\alpha_{7,15}$ and $\alpha_{11,2}$). True values are represented by the diamond shape in (b) and (c).

$S_n(x)$ and $S_m(y)$ are equally spaced knots *fifth*-order B-spline functions for x and y, respectively, given by [34, eq. 6], and Appendix B

$$S_n(x) = s^{(5)}(x - x_n), S_m(y) = s^{(5)}(y - y_m), \quad x_{\min} \le x \le x_{\max}, y_{\min} \le y \le y_{\max}. \tag{6b}$$

Notice that a *fifth*-order B-spline function is represented by a piecewise fourth-order polynomial [50]. The expressions for $s^{(5)}$, x_n, and y_m are given in Appendix B.

In this example, the true surface is modeled using the B-spline function of (6a), with all coefficients $\alpha_{n,m}$ as random numbers

generated using a computer random generator from uniform distribution. The produced random rough surface is enforced to have a zero mean height. The total number of coefficients is $16 \times 16 = 256$, assuming $N_n = N_m = 12$. For simplicity, 254 coefficients are assumed known, while only two coefficients are unknown. The inversion algorithm is tested to recover the unknown coefficients $\alpha_{7,15}$ and $\alpha_{11,2}$, as shown in Fig. 2(c). Zero initial values of $\alpha_{7,15}$ and $\alpha_{11,2}$ are used in the inversion algorithm.

D. Computational Requirements

In Examples 1 and 2, the inversion algorithm required 76 and 88 runs of the 3-D SDFMM forward solver to achieve 10^{-6} error in the cost function, for the sinusoidal and tensor-product B-spline surface, respectively. Each run required 231 MB of computer memory and approximately 15 CPU min, to achieve tolerance of 10^{-3} of the transpose-free quasi-minimal residual algorithm (TFQMR) iterative solver. A surface discretization distance of $0.08\lambda_0$ is used for all the cases in this paper at $f = 1$ GHz. All computational work is conducted using the COMPAQ ALPHA 667-MHz server.

III. Numerical Results

In this section, several numerical examples of reconstructing the profile of groove-like random rough surfaces are presented [see Fig. 3(a)]. All results presented in this section are for ground surface of dimensions 1.0×1.0 m ^{2} and relative dielectric constant $\varepsilon_r = 4.0 - i0.01$ (realistic dry soil [34]–[37]). The incident wave is a Gaussian beam illuminating a circular spot of diameter 40 cm in the x-y plane on the ground [see Fig. 3(a)]. This implies that a 3-D scattering mechanism is involved in the inversion algorithm, where all fields are computed using the SDFMM code. The random rough surface is approximated by the 1-D B-spline function, $h(x) \approx \sum_{n=-4}^{N_n-1} \alpha_n S_n(x)$, where $S_n(x)$ is a *fifth*-order B-spline function given in (6b) and in Appendix B, with $N_n = 12$ leading to a number of unknown coefficients $\alpha_n = 16$, as discussed in Section II. In all results presented here, true surfaces are generated using the above B-spline function, with 16 random number coefficients obtained using a computer random generator from uniform distribution. Also, all true random rough surfaces are enforced to have zero mean height. The random coefficients are appropriately normalized to generate rough surfaces with *a priori* assumption of the surface height range, i.e., minimum to maximum heights. The height ranges considered here are 6 cm in Figs. 3–8 (similar to the work reported in [34]–[37]), 12 cm in Fig. 9(a) and (b), and 15 cm in Fig. 9(b) and (c). These values are used to define the lower and upper constraints $\theta_{\mathrm{LB}} \le \theta \le \theta_{\mathrm{UB}}$, e.g., for the 6-cm surface height case, the lower and upper limits are -3 and 3 cm, respectively, for all coefficients.

In Fig. 3(b)–(f), the inversion algorithm is tested to reconstruct the profile of the rough surface based on received data with y-polarized fields at 11 receivers located at 15 cm above the ground mean plane and separated by 6 cm (between $x = 20.4$ and $x = 80.4$ cm). The gradient of the cost function c in (5b) is evaluated in this example using the central difference equation [49]. The cost function $C_1(\theta)$ in (1) is used in this example. Data obtained based on a multiple-incidence strategy at a single frequency ($f = 1$ GHz) are employed in the inversion algorithm. Instead of using the data at all receivers and all incident angles simultaneously, we only use the data at all receivers simultaneously, but for one incident angle at a time, while updating the cost function after each determination of the parameters corresponding to each incident angle. This procedure can be considered as *marching on in angle*, and it is, in a way, similar to the nonlinear *Kaczmarz-type* approach used by Dorn *et al.* [48]. Our algorithm begins with zero initial values of the unknown coefficients (i.e., flat surface) at normal incidence for two inversion iterations as shown in Fig. 3(b). The output values of the coefficients are then used as initial values in the

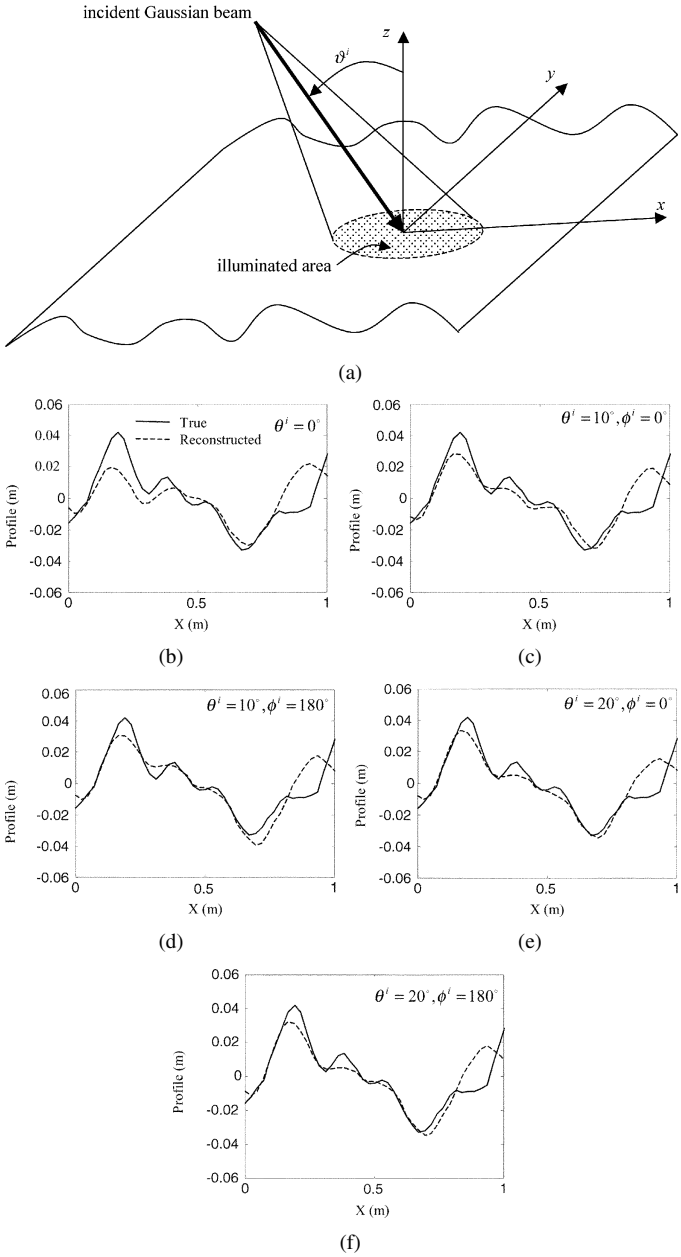

Fig. 3. (a) Groove-like rough surface illuminated in the x–y plane by a 2-D Gaussian beam. (b)–(f) Reconstruction of rough surface using five points of multiple-incidence strategy at $f = 1$ GHz, (b) normal incidence, (c) $\vartheta^i = 10^\circ$, $\varphi^i = 0$, (d) $\vartheta^i = 10^\circ$, $\varphi^i = \pi$, (e) $\vartheta^i = 20^\circ$, $\varphi^i = 0$, and (f) $\vartheta^i = 20^\circ$, $\varphi^i = \pi$. Each incident angle was run for two inversion iterations.

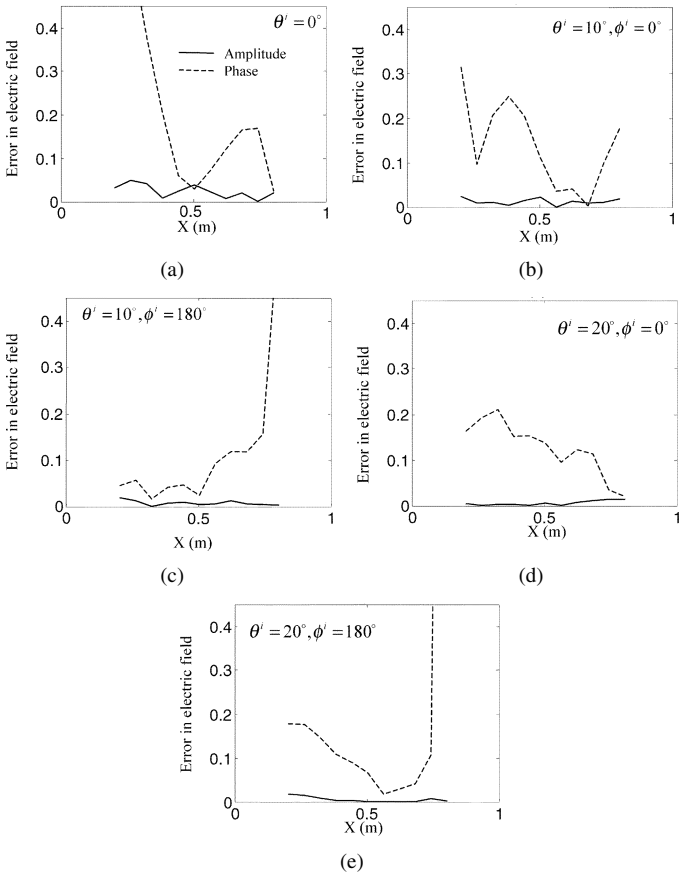

Fig. 4. Absolute error between electric field scattered from true surface and electric field scattered from reconstructed surface of Fig. 3(b)–(f). (a) Normal incidence. (b) $\vartheta^i = 10°$, $\varphi^i = 0$. (c) $\vartheta^i = 10°$, $\varphi^i = \pi$. (d) $\vartheta^i = 20°$, $\varphi^i = 0$, and (e) $\vartheta^i = 20°$, $\varphi^i = \pi$. (Solid line) Amplitude. (Dotted line) Phase.

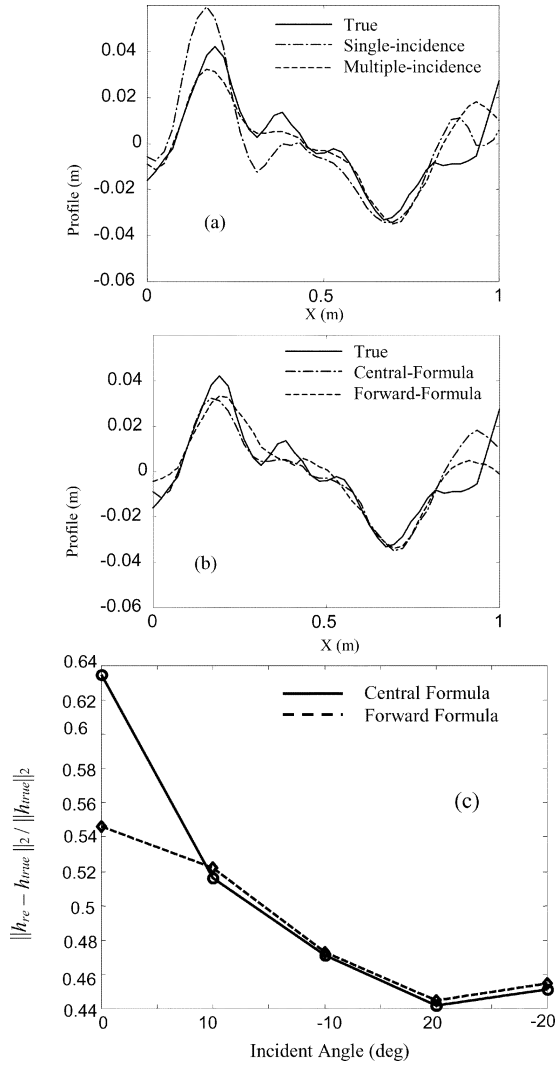

Fig. 5. (a) and (b) Surface profile reconstruction. (a) Comparison between single-incidence at normal and multiple-incidence. (b) Comparison between central-formula and forward-formula gradients (multiple-incidence of Fig. 3). $f = 1$ GHz and ten total number of inversion iterations used in this case. (c) Error criterion ($\|h_{\rm re} - h_{\rm true}\|_2 \,/\, \|h_{\rm true}\|_2$) versus the incident angle for the multiple-incidence results shown in Fig. 3(b)–(f) and (b) for (solid line) the gradient central formula and (dashed line) forward formula, respectively, at $f = 1$ GHz. Notice that each point in the plot represents the error when that incident angle is used in *a marching-on* scheme in conjunction with all the other incident angles to the left of that point. The positive and negative incident angles indicate to $\varphi^i = 0$, and $\varphi^i = \pi$, respectively.

algorithm at $\vartheta^i = 10°$, $\phi^i = 0$ for two inversion iterations, as shown in Fig. 3(c). This process is repeated at the incident angles $\vartheta^i = 10°$, $\phi^i = \pi$, followed by $\vartheta^i = 20°$, $\phi^i = 0$, and $\vartheta^i = 20°$, $\phi^i = \pi$, as shown in Fig. 3(d)–(f), respectively. The estimated spline coefficients at one angle are used to manually update the initial guess at the succeeding angle. Two iterations were chosen at each angle, based on several numerical results (not presented here), showing slight improvement in the reconstruction when more iterations are used. Fig. 3(b)–(f) show good results in the profile reconstruction upon implementing the multiple-incidence strategy. In addition, the results of Fig. 3 show that the small roughness features of the surface were not accurately recovered, as will be discussed later in this section. In the current example ($f = 1$ GHz), each inversion iteration required 56–65 runs of the 3-D SDFMM forward solver, where each run required, on the average, 11 CPU min, to achieve a TFQMR tolerance of 10^{-2}, and 165 MB of computer memory.

In Fig. 4(a)–(e), a comparison between the magnitude and phase of the electric field scattered from the true surface and from the estimated surface is shown, for the same data of Fig. 3 where the cost function $C_1(\theta)$ was used. Notice that the error in the phase (dashed line) is always larger than the error in the magnitude (solid line), as will be discussed later in this section. Also, notice that the error in the amplitude is diminishing in Fig. 4(e) compared with Fig. 4(a). In this example, the beamwidth limits are $x = 30$–70 cm, and the 11 receivers are located between $x = 20.4$ –80.4 cm.

A comparison between the single- and multiple-incidence strategies at $f = 1$ GHz is shown in Fig. 5(a). These results are obtained using a total of ten inversion iterations for the same cost function and central-difference gradient formula of Fig. 3. The results of Fig. 5(a) clearly show that the multiple-incidence strategy provides a better reconstruction of the surface profile. Another important issue in the inversion algorithm is the required CPU time, which can be tremendously improved by implementing the forward-difference formula for the gradient, as shown in Fig. 5(b). The results are obtained upon running the inversion algorithm for a total of ten iterations at $f = 1$ GHz, using the same multiple-incidence strategy of Fig. 3. The results

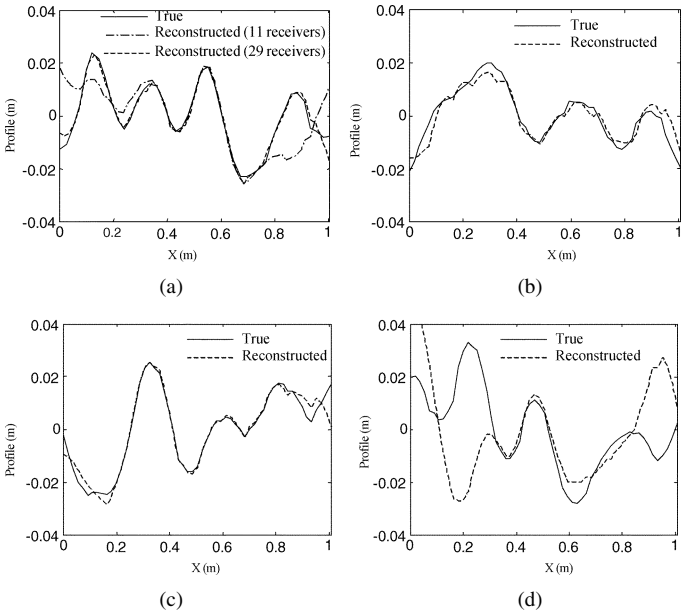

Fig. 6. Reconstruction of four surface profiles using single incidence ($\vartheta^i = 0$) and single frequency (2 GHz). The 29 receivers are located at 7.5 cm above the ground mean plane separated by 3 cm. All results are obtained after total of ten inversion iterations.

show insignificant difference between the reconstructed surface profile based on the central-difference formula compared with that based on the forward-difference formula, especially within the beamwidth limits ($x = 0.3$ to 0.7 m). Notice that the central-difference formula of the gradient required evaluating the 3-D scattering problem 56–65 times/inversion iteration, compared with 27–34 runs upon implementing the forward-difference formula. This approach has lead to substantial saving in the CPU time. Therefore, the forward-difference formula is adopted in the remainder of this paper.

To demonstrate the enhancement in profile reconstructions, upon using the multiple-incidence strategy, in Figs. 3 and 5, an error criterion defined by the quantity $\|h_{\rm re} - h_{\rm true}\|_2 / \|h_{\rm true}\|_2$ is adopted. The error is plotted in Fig. 5(c) versus the incident angle, following the same order of angles used in the strategy. The quantities $h_{\rm re}$ and $h_{\rm true}$ represent the reconstructed and the true surface profiles, respectively. Notice that each point in the plot represents the error when that incident angle is used in a *marching-on* scheme in conjunction with all the other incident angles to the left of that point. The positive and negative signs of the incident angles in Fig. 5(c) indicate to $\varphi^i = 0$ and $\varphi^i = \pi$, respectively. In addition, Fig. 5(c) shows a comparison between the gradient central formula of Fig. 3(b)–(f), and the gradient forward formula of Fig. 5(b), for the multiple-incidence case. The results of Fig. 5(c) clearly show the reduction in the error upon using the multiple-incidence strategy. In addition, it shows the insignificant difference in the error upon using the forward versus the central formula, except at normal incidence. The forward formula, unexpectedly, shows better results than the central formula at normal incidence.

As mentioned earlier, the results of Figs. 3 and 4 show inaccurate reconstruction of the surface small-scale roughness, implying the need for higher frequencies, to be demonstrated in Figs. 6 and 7. In addition, using the cost function $C_2(\theta)$ instead of $C_1(\theta)$, given in (1), has shown better profile reconstruction, since it implicitly accounts for the phase information of the scattered electric fields. Therefore, the function $C_2(\theta)$ will be adopted in the remainder of this paper. However, the numerical results show that using $C_1(\theta)$ or $C_2(\theta)$ still demonstrate smaller error in the electric field amplitudes compared with the phase, similar to Fig. 4. This issue may be resolved by using a new cost function of appropriate weights of the phase and magnitude, which is not in the scope of this paper.

The results of Fig. 6(a)–(d) demonstrate the reconstruction of four different rough surfaces with profiles dominated by small-scale roughness. Single-incidence in the normal direction is used here at $f = 2$ GHz. The number of receivers is increased to 29 instead of 11 receivers. In Fig. 6(a), the 29 receivers are located between $x = 8.4$ cm and $x = 92.4$ cm, while the 11 receivers are located between $x = 35.4$ and $x = 65.4$ cm. In both cases, the receivers are located at 7.5 cm above the ground mean plane with separation distance of 3 cm. The results of Fig. 6(a)–(c) show good agreement with the true surface profile, even outside the limits of the beamwidth (i.e., outside $x = 0.3$ to 0.7 m). Also, the profile-reconstruction obtained using the 11 receivers is compared with using the 29 receivers in Fig. 6(a), demonstrating the improvement obtained by increasing the number of receivers. However, the profile reconstruction in Fig. 6(d) does not show good agreement with the true profile, almost everywhere.

In this case, the multiple-incidence strategy at a single frequency (2 GHz) is implemented trying to improve the profile reconstruction, as shown in Fig. 7(a). Similar to Fig. 3, the reconstruction algorithm begins at normal incidence with zero initial values of the coefficients (i.e., flat surface). The algorithm is executed for two inversion iterations at $\vartheta^i = 0$, followed by two iterations at each of the angles: $\vartheta^i = 10°$, $\phi^i = 0$, $\vartheta^i = 10°$, $\phi^i = \pi$, $\vartheta^i = 20°$, $\phi^i = 0$, and $\vartheta^i = 20°$, $\phi^i = \pi$ (*marching-on in angle*). The estimated coefficients at each incident angle are used as initial values for the succeeding angle, etc. The results in Fig. 7(a) show better profile reconstruction, upon implementing the multiple-incidence strategy. To achieve realistic CPU time, a range of surface discretization distances of $0.08\lambda_0$ to $0.12\lambda_0$ was experimented at $f = 1.5$ to 2 GHz, leading to use $0.12\lambda_0$ discretization for the 1.5–2-GHz cases. In Fig. 6(d), each inversion iteration involved 30 runs of the 3-D SDFMM forward solver, where each run required, on the average, 18 CPU min to achieve a TFQMR tolerance of 10^{-2} and 148 MB of computer memory.

To improve the results of Fig. 7(a), instead of using the data at all receivers, all incident angles, and all frequencies simultaneously, we only use the data at all receivers simultaneously, but for one frequency at a time followed by one incident angle at a time. The cost function $C_2(\theta)$ is updated after each determination of the coefficients corresponding to each frequency and each incident angle. This combined approach, multifrequency/multiple-incidence, can be referred to as *marching-on in frequency/angle* and is implemented again for the profile of Fig. 6(d). The scheme begins with running the inversion algorithm using data at 1 GHz and normal incidence for two iterations [Fig. 7(b)], followed by using data at 1.5 GHz and normal incidence for two iterations [Fig. 7(c)], then data at

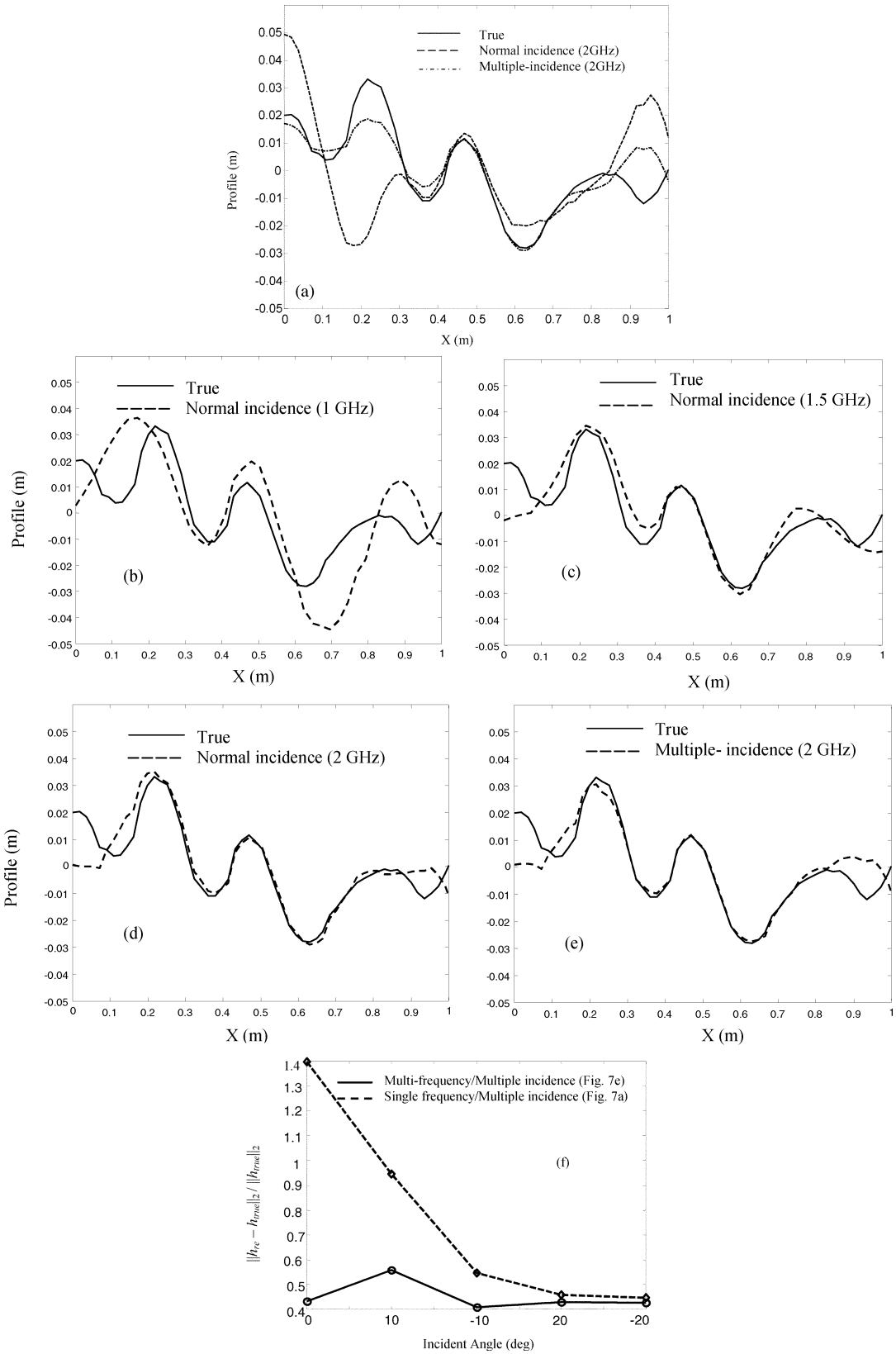

Fig. 7. (a) Reconstruction of surface profile in Fig. 6(d) using five points of multiple-incidence strategy at $\vartheta^i = 0$; $\vartheta^i = 10°$, $\phi^i = 0$; $\vartheta^i = 10°$, $\phi^i = \pi$; $\vartheta^i = 20°$, $\phi^i = 0$; and $\vartheta^i = 20°$, $\phi^i = \pi$ at 2 GHz. The 29 receivers are located at 7.5 cm above the ground mean plane separated by 3 cm. (b)–(e) Reconstruction of surface profile in Fig. 6(d) using multiple-frequency strategy at (b) 1 GHz, (c) 1.5 GHz, (d) 2 GHz at $\vartheta^i = 0$, followed by five points of multiple-incidence strategy at (e) $\vartheta^i = 0$; $\vartheta^i = 10°$, $\phi^i = 0$; $\vartheta^i = 10°$, $\phi^i = \pi$; $\vartheta^i = 20°$, $\phi^i = 0$; and $\vartheta^i = 20°$, $\phi^i = \pi$ at 2 GHz. The 29 receivers are located at 7.5 cm above the ground mean plane separated by 3 cm. (f) Error criterion $\|h_{\rm re} - h_{\rm true}\|_2 \,/\, \|h_{\rm true}\|_2$ versus the incident angle when using multiple incidence at (dashed line) single frequency (2 GHz) as shown in (a), and when using the multifrequency followed by (solid line) multiple-incidence as shown in (e). Notice that each point in the plot represents the error when that incident angle is used in a *marching-on* scheme in conjunction with all the other incident angles to the left of that point. The positive and negative incident angles in (f) indicate to $\varphi^i = 0$ and $\varphi^i = \pi$, respectively.

2 GHz and normal incidence for two iterations [Fig. 7(c)]. Zero initial guess of the spline coefficients is assumed in Fig. 7(b), then after two inversion iterations at 1 GHz, the estimated coefficients are used as initial guess in Fig. 7(c), and again after two inversion iterations at 1.5 GHz, the estimated coefficients are used as initial guess in Fig. 7(d) for two inversion iterations at 2 GHz. Then, in Fig. 7(e), the multiple incidence is implemented with initial guess equal to the estimated coefficients of Fig. 7(d) at normal incidence, followed by the same sequence of incident angles as used in Fig. 7(a) (five points). The results of Fig. 7(e) show good agreement with the true surface profile upon implementing the multifrequency strategy, followed by the multiple-incidence strategy [same five points of Fig. 7(a)], all at 2 GHz. In addition, comparing the results of Fig. 7(d) (multifrequency at normal incidence) with those of Fig. 6(d) (single frequency at normal incidence) apparently shows reconstruction improvement due to the multifrequency strategy.

Fig. 7(f) shows the error $||h_{\rm re} - h_{\rm true}||_2 \,/\, ||h_{\rm true}||_2$ for the results of Fig. 7(a), when implementing the single frequency/multiple-incidence (dashed line), demonstrating the error reduction upon *marching-on in angle*. The results show additional error reduction upon implementing the multifrequency followed by the multiple-incidence (solid-line), shown in Fig. 7(f). Notice that in Fig. 7(f), the error is slightly changing between the fourth and fifth incident angles, i.e., $\vartheta^i = 20°$, $\phi^i = 0$ and $\vartheta^i = 20°$, $\phi^i = \pi$, respectively. In Fig. 7(f), each point in the plot represents the error when that incident angle is used in *a marching-on* scheme in conjunction with all the other incident angles to the left of that point.

In the above results of Figs. 3, 5, 6(d), and 7(a), consistent errors were observed near the edges of the surface. In some cases, the error is more pronounced near one edge more than the other, e.g., in Fig. 3(b)–(f), the error is larger between $x = 0.8$ to 1.0 m, while in Fig. 7(a), it is larger between $x = 0$ to 0.3 m. The same observation was reported by Galdi *et al.* [34]–[37]. This is due to using numerical methods for profile reconstruction, where the incident waves near the edges are deliberately minimized to eliminate artificial edge effects (~ -30 dB here). This approach leads to minimize the scattered waves from the near-edge regions and, consequently, to produce inaccurate retrieval of the profile at these regions. In some cases, these errors are reduced upon increasing the number of receivers, as shown in Fig. 6(a), where the number of receivers is increased from 11 to 29. The results of Fig. 6(d) show inaccurate reconstruction almost everywhere, but more pronounced near the left edge ($x = 0$ to 0.3 m). As mentioned earlier, Fig. 7(a) shows improved profile reconstruction than Fig. 6(d), upon applying the multiple incidence, except near the right edge ($x = 0.8$ to 1.0 m). Although, these errors are minimized in Fig. 7(e), they are not completely eliminated [34]–[37].

Our ultimate goal of estimating the unknown profile of the rough ground surface is to remove the clutter due to the rough surface from the data, e.g., in the mine detection application. The upper plot in Fig. 8 shows a 3-D spheroid target of dimensions $9 \times 9 \times 4.5$ cm^3, buried at $z = -4.5$ cm under the rough profile of Fig. 6(a). In this figure, there are only 11 receivers located at $z = 7.5$ cm above ground with separation

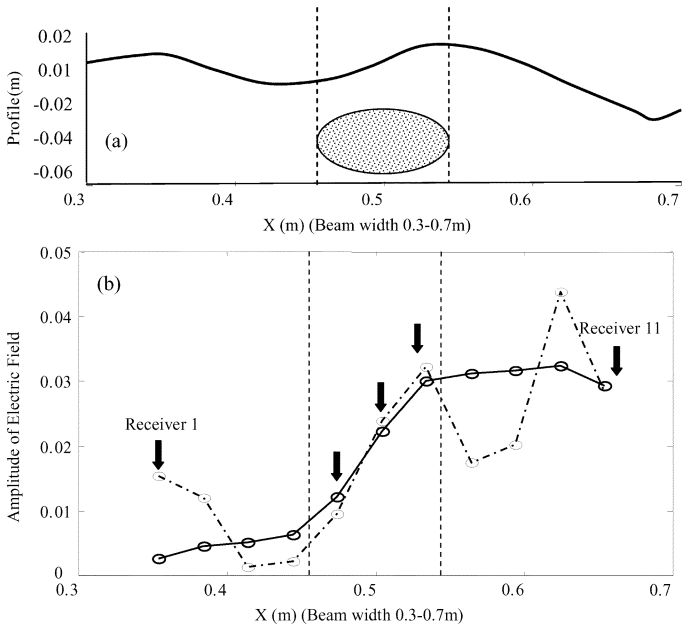

Fig. 8. (a) Three-dimensional spheroid target of dimensions $9 \times 9 \times 4.5$ cm^3, buried at $z = -4.5$ cm under the rough surface of Fig. 6(a). (b) Ideal and estimated target signatures, where total of 11 receivers are used.

of 3 cm, between $x = 35.4$ cm and $x = 65.4$ cm. All results here are at normal incidence. The lower plot shows the target signature obtained by subtraction. The electric field scattered from the true surface *with the buried target* represents the true data. The electric field scattered from the true surface or from the estimated surface profile, *with no buried target*, is subtracted from the true data. The solid line in Fig. 8(b) represents the ideal target signature (i.e., surface known), while the dashed–dotted line represents the estimated target signature (i.e., surface estimated). The estimated profile is obtained based on the single-frequency strategy (2 GHz) and single incidence ($\vartheta^i = 0°$). The results show that the estimated signature is in reasonable agreement with the ideal signature only at receivers 5–7, located right above the target. The target signature looks asymmetric in Fig. 8(b) due to the asymmetry of the random rough surface profile.

In all the cases shown in Figs. 3–8, the surface height ranges from minimum ~ -3 cm to maximum ~ 3 cm (i.e., 6-cm height range), which is increased to 12-cm range in Fig. 9(a) and (b) and 15-cm range in Fig. 9(c)–(d). The 29 receivers are positioned above the ground, between $x = 8.4$ cm and $x = 92.4$ cm, at $z = 10$ cm in Fig. 9(a) and (b) and at $z = 15$ cm in Fig. 9(c) and (d), with separation distance of 3 cm. Fig. 9(a) shows the reconstruction results for the 12-cm height surface at 1 GHz using the marching-on in angles at seven points ($\vartheta^i = 0°$; $\vartheta^i = 10°$, $\phi^i = 0$; $\vartheta^i = 10°$, $\phi^i = \pi$; $\vartheta^i = 20°$, $\phi^i = 0$; $\vartheta^i = 20°$, $\phi^i = \pi$; $\vartheta^i = 30°$, $\phi^i = 0$; and $\vartheta^i = 30°$, $\phi^i = \pi$). In Fig. 9(a), the surface height range is ~ 12 cm with $f = 1$ GHz and zero initial guess of the coefficients at $\vartheta^i = 0°$. The same strategy, discussed earlier, for updating the initial guess of the coefficients at each succeeding angle is implemented. In Fig. 9(b), the frequency is increased to 2 GHz and the *marching-on* in angle is repeated using the same data of Fig. 9(a). In Fig. 9(c), the surface height range is increased

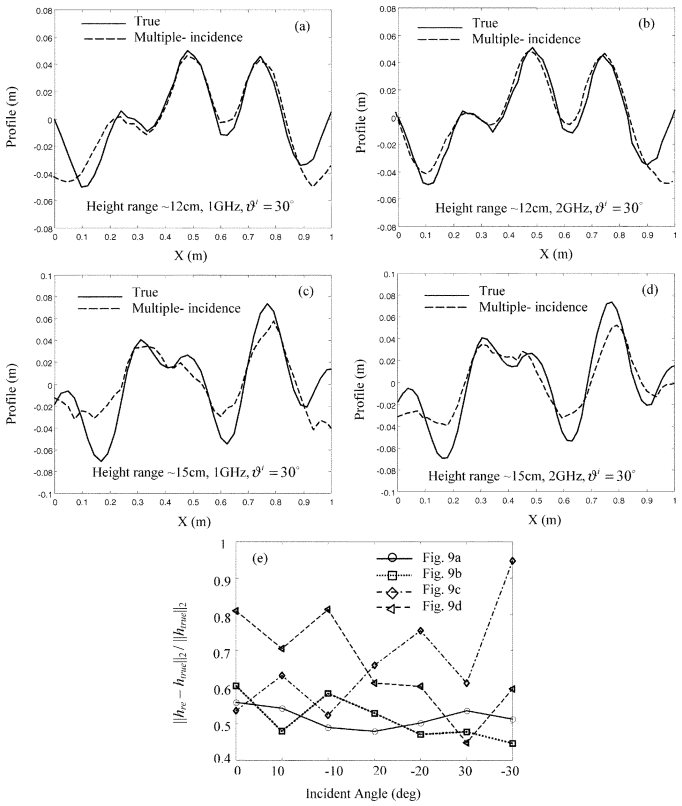

Fig. 9. Reconstruction of rougher surface profiles using seven points of multiple-incidence strategy $\vartheta^i = 0$; $\vartheta^i = 10^\circ$, $\phi^i = 0$; $\vartheta^i = 10^\circ$, $\phi^i = \pi$; $\vartheta^i = 20^\circ$, $\phi^i = 0$; $\vartheta^i = 20^\circ$, $\phi^i = \pi$; $\vartheta^i = 30^\circ$, $\phi^i = 0$; and $\vartheta^i = 30^\circ$, $\phi^i = \pi$ for surface height range as (a) $\sim$ 12 cm (1 GHz) zero initial guess; (b) $\sim$ 12 cm (2 GHz), with initial guess equal to the estimated coefficients in (a); (c) $\sim$ 15 cm (1 GHz) with zero initial guess; and (d) $\sim$ 15 cm (2 GHz) with initial guess equal to the estimated coefficients in (c). (e) Error criterion $\|h_{\rm re} - h_{\rm true}\|_2 / \|h_{\rm true}\|_2$ for the cases shown in (a)–(d). The positive and negative signs of incident angles indicate $\varphi^i = 0$ and $\varphi^i = \pi$, respectively. The results in (a)–(d) are for $\vartheta^i = 30^\circ$ and $\phi^i = 0$.

to $\sim$ 15 cm with $f = 1$ GHz and zero initial guess of the coefficients at $\vartheta^i = 0^\circ$. The *marching-on* in angle using the same seven points of Fig. 9(a) is repeated. In Fig. 9(d), the frequency is increased to 2 GHz, and the *marching-on* in angle is repeated using the same data of Fig. 9(c). The error criterion $\|h_{\rm re} - h_{\rm true}\|_2 / \|h_{\rm true}\|_2$ for the cases shown in Fig. 9(a)–(d) is presented in Fig. 9(e). The reconstructed profiles in Fig. 9(a)–(d) are shown for $\vartheta^i = 30^\circ$ and $\phi^i = 0$. Although reasonable reconstruction of the surface is still observed in Fig. 9(c) and (d) at the 15-cm-height case, especially at 2 GHz, however, the results are not as good as those for the 6-cm (shown earlier) or the 12-cm-height case shown in Fig. 9(a) and (b). This could be interpreted due to a nonnegligible amount of multiple scattering associated with rougher surfaces. In this paper, both the synthetic and simulated data are obtained using the SDFMM, which accounts for all multiple-scattering mechanisms form the rough surface. This was not the case in the work reported in [34]–[37] or [38], where the synthetic and simulated data were obtained using the Kirchhoff approximation, which accounts only for the single scatter from rough surface [13]. The influence of increasing surface roughness on deteriorating profile reconstruction or inferring of surface parameters, using other techniques, were also reported in the literature [25], [29], [30]–[33]. In Fig. 9(e), the results show that for the case of 12 cm at 1 GHz, the error is slightly fluctuating upon *marching-on* in angle, while at 2 GHz, the error is also fluctuating but with a tendency to decrease with angle. For the case of 15 cm at 1 GHz, more fluctuations in the error is observed but with tendency to increase upon *marching-on* in angle, while at 2 GHz, the error is still fluctuating but with tendency to decrease with angle. The required computer memory in Fig. 9(a)–(d) is 165 and 157 MB for the 1- and 2-GHz cases, as previously discussed. The average CPU time per run for the cases shown in Fig. 9(a)–(d) is 8.4, 16, 8.6, and 18 min, respectively. On the average, 32–35 SDFMM runs were required per inversion iteration.

Although all examples shown in this paper are for the horizontal copolarized waves, the presented algorithm can handle the fully polarimteric case, where any of the co- or cross- polarized waves can be employed in the inversion technique (i.e., HH, VV, HV, VH) [52]. The fully polarimetric capability of the inversion algorithm will be helpful in imaging small targets buried under the rough ground, which will be the subject of a future work.

IV. Concluding Remark

A fast computational inversion algorithm is presented in this paper based on the SDFMM fast forward solver combined with the Fletcher and Powell searching technique. The issues of wave direction, computational aspects, receiver locations and number, gradient numerical formula, and surface roughness are investigated. The results show that implementing the multifrequency strategy demonstrates good improvement in the surface profile reconstruction. In addition, the profile reconstruction has been improved upon implementing the multiple-incidence strategy even at single frequency. Deterioration in surface reconstruction is observed as surface roughness increases, which could be due to a nonnegligible amount of surface multiple scattering. The results presented in this paper were produced in realistic time because of two main factors: 1) the efficient 3-D fast forward solver (SDFMM) and 2) the optimized Fletcher and Powell searching algorithm.

In this paper, we presented results indicating that *marching-on* methods offer a feasible approach to provide high-quality reconstruction of rough surfaces. More work need to be conducted to address the more general questions concerning synthesizing specific iterative strategies for nonlinear problems to guarantee some level of convergence.

Appendix A

The integro-differential operators are given by [41]–[43]

$$L_{1,2}\overline{X}(\overline{r}) = \int_{S_1} \Big\{ i\omega\mu_{1,2}\Phi_{1,2}\overline{X}(\overline{r}') + \frac{i}{\omega\varepsilon_{1,2}} \cdot \nabla\nabla' \cdot \overline{X}(\overline{r}')\,\Phi_{1,2} \Big\} ds', \qquad \overline{r} \in S_1 \quad \text{(A1)}$$

$$K_{1,2}\overline{X}(\overline{r}) = \int_{S_1} \overline{X}(\overline{r}') \times \nabla\Phi_{1,2} ds', \qquad \overline{r} \in S_1. \quad \text{(A2)}$$

The vector $\overline{X}(\cdot)$ represents the surface electric or magnetic currents, $\overline{J}$ and $\overline{M}$, respectively. The intrinsic impedances $\eta_1 = \sqrt{\mu_1/\varepsilon_1}$ and $\eta_2 = \sqrt{\mu_2/\varepsilon_2}$ are for the air and ground material,

respectively. The permittivity and permeability are $\varepsilon_1 = \varepsilon_0$ and $\mu_1 = \mu_0$ for the air and ε_2 and μ_2, for the ground. The 3-D scalar Green's function is

$$\Phi_i = \frac{\exp\left(-ik_i\left|\overline{r}-\overline{r}'\right|\right)}{4\pi\left|\overline{r}-\overline{r}'\right|}, \qquad i=1,2 \tag{A3}$$

where $k_i = \omega\sqrt{\varepsilon_i\mu_i}$ is the wavenumber, and $\overline{r}'$ and $\overline{r}$ are the source and observation points, respectively. The impedance matrix $\overline{\overline{Z}}$ is given by [41]–[43]

$$\overline{\overline{Z}} = \begin{pmatrix} \left\langle \overline{j}, (L_1+L_2)\,\overline{j}\right\rangle_{S_1} & \left\langle \overline{j}, -\eta_1\,(K_1+K_2)\,\overline{j}\right\rangle_{S_1} \\ \left\langle \overline{j}, \eta_1\,(K_1+K_2)\,\overline{j}\right\rangle_{S_1} & \left\langle \overline{j}, \eta_1^2\left(\frac{L_1}{\eta_1^2}+\frac{L_2}{\eta_2^2}\right)\overline{j}\right\rangle_{S_1} \end{pmatrix}. \tag{A4}$$

The symbol $\left\langle \overline{A}, \overline{B}\right\rangle_S = \int_S \overline{A}^* \cdot \overline{B} ds$ denotes the complex inner product between vector functions $\overline{A}$ and $\overline{B}$ on a surface S. The matrix $\overline{\overline{Z}}$ in (A4) is a $2N \times 2N$ matrix, where $2N$ is the total number of unknown surface current coefficients $\overline{I}$ [41]–[43].

APPENDIX B

The equally spaced knots *fifth*-order B-spline function $s^{(5)}(X)$ is given by [34], [50], [51]

$$s^{(5)}(X) = \begin{cases} \left(\frac{8}{115}\right)X^4, & 0 \le X < 1 \\ \left(\frac{-8}{115}\right)(5-20X+30X^2-20X^3+4X^4), & 1 \le X < 2 \\ \left(\frac{8}{115}\right)(155-300X+210X^2-60X^3+6X^4), & 2 \le X < 3 \\ \left(\frac{-8}{115}\right)(655-780X+330X^2-60X^3+4X^4), & 3 \le X < 4 \\ \left(\frac{8}{115}\right)(X-5)^4, & 4 \le X < 5 \end{cases} \tag{B1}$$

in which X is $(x-x_n)/\Delta x$ or $(y-y_m)/\Delta y$, and x_n and y_m are given by

$$\begin{aligned} x_n &= x_{\min} + n\Delta x \\ y_m &= y_{\min} + m\Delta y \\ \Delta x &= \frac{(x_{\max}-x_{\min})}{N_n} \\ \Delta y &= \frac{(y_{\max}-y_{\min})}{N_m}. \end{aligned} \tag{B2}$$

The minimum and maximum values of x and y in (B2) are $x_{\min} = y_{\min} = -0.5$, $x_{\max} = y_{\max} = 0.5$.

REFERENCES

[1] A. Ishimaru and J. S. Chen, "Scattering from very rough metallic and dielectric surfaces: A theory based on the modified Kirchhoff approximation," *Waves Random Media*, pp. 21–34, Jan. 1991.

[2] P. Tran and A. A. Maradudin, "Scattering of a scalar beam from a two-dimensional randomly rough hard wall: Enhanced backscatter," *Phy. Rev. B*, vol. 45, no. 7, pp. 3936–3939, Feb. 1992.

[3] M. Nieto-Vesperinas and J. A. Sánchez-Gil, "Intensity angular correlations of light multiply scattered from random rough surfaces," *J. Opt. Soc. Amer. A*, vol. 10, no. 1, pp. 150–157, Jan. 1993.

[4] M. El-Shenawee and E. Bahar, "Numerical method to compute TE and TM multiple scatter from rough surfaces exhibiting backscatter enhancement," *IEEE Trans. Magn.*, vol. 30, pp. 3140–3143, Sept. 1994.

[5] K. Fung, M. R. Shah, and S. Tjuatja, "Numerical simulations of scattering from three-dimensional randomly rough surfaces," *IEEE Trans. Geosci. Remote Sensing*, vol. 32, pp. 986–994, Sept. 1994.

[6] L. Tsang, C. H. Chan, K. Pak, H. Sangani, A. Ishimaru, and P. Phu, "Monte Carlo simulations of large-scale composite random rough-surface scattering based on the banded-matrix iterative approach," *J. Opt. Soc. Amer. A*, vol. 11, no. 2, pp. 691–696, Feb. 1994.

[7] E. Bahar and M. El-Shenawee, "Enhanced backscatter from one dimensional random rough surfaces-stationary phase approximations to full wave solutions," *J. Opt. Soc. Amer. A*, vol. 12, no. 1, pp. 151–161, Jan. 1995.

[8] F. D. Hastings, J. B. Schneider, and S. L. Broschat, "A Monte Carlo FDTD technique for rough surface scattering," *IEEE Trans. Antennas Propagat.*, vol. 43, pp. 1183–1191, Nov. 1995.

[9] D. A. Kapp and G. S. Brown, "A new numerical method for rough surface scattering calculations," *IEEE Trans. Antennas Propagat.*, vol. 44, pp. 711–721, May 1996.

[10] J. T. Johnson, L. Tsang, R. T. Shin, K. Pak, C. H. Chan, A. Ishimaru, and Y. Kuga, "Backscattering enhancement of electromagnetic waves from two-dimensional perfectly conducting random rough surfaces: A comparison of Monte Carlo simulations with experimental data," *IEEE Trans. Antennas Propagat.*, vol. 44, pp. 748–756, May 1996.

[11] R. L. Wagner, J. Song, and W. C. Chew, "Monte Carlo simulation of electromagnetic scattering from two-dimensional random rough surfaces," *IEEE Trans. Antennas Propagat.*, vol. 45, pp. 235–245, Feb. 1997.

[12] C. H. Chan, L. Tsang, and Q. Li, "Monte Carlo simulations of large-scale one dimensional random rough-surface scattering at near grazing incidence: Penetrable case," *IEEE Trans. Antennas Propagat.*, vol. 46, pp. 142–149, Jan. 1998.

[13] E. Thorsos, "The validity of the Kirchhoff approximation for rough surface scattering using a Gaussian roughness spectrum," *J. Acoust. Soc. Amer.*, vol. 83, no. 1, pp. 78–92, 1988.

[14] M. El-Shenawee and C. Rappaport, "Modeling clutter from Bosnian and Puerto Rican rough ground surfaces for GPR subsurface sensing applications using the SDFMM technique," *J. Subsurf. Sens. Technol. Appl.*, vol. 2, no. 3, pp. 249–264, July 2001.

[15] M. El-Shenawee, C. Rappaport, E. Miller, and M. Silevitch, "Three-dimensional subsurface analysis of electromagnetic scattering from penetrable/PEC objects buried under rough surfaces: Use of the steepest descent fast multipole method (SDFMM)," *IEEE Trans. Geosci. Remote Sensing*, vol. 39, pp. 1174–1182, June 2001.

[16] M. El-Shenawee, C. Rappaport, and M. Silevitch, "Monte Carlo simulations of electromagnetic wave scattering from random rough surface with 3-D penetrable buried object: Mine detection application using the SDFMM," *J. Opt. Soc. Amer. A*, vol. 18, no. 12, pp. 3077–3084, Dec. 2001.

[17] M. El-Shenawee, "Scattering from multiple objects buried under two-dimensional randomly rough surface using the steepest descent fast multipole method," *IEEE Trans. Antennas Propagat.*, vol. 51, pp. 802–809, Apr. 2003.

[18] M. El-Shenawee and C. Rappaport, "Monte Carlo simulations for the statistics of clutter in minefields: AP mine-like target buried near a dielectric object beneath two-dimensional randomly rough ground," *IEEE Trans. Geosci. Remote Sensing*, vol. 40, pp. 1416–1426, June 2002.

[19] D. Jiang, W. Meleis, M. El-Shenawee, E. Mizan, M. Ashouei, and C. Rappaport, "Parallel implementation of the steepest descent fast multipole method (SDFMM) on a Beowulf cluster for subsurface sensing applications," *Microwave Wireless Comp. Lett.*, vol. 12, no. 1, pp. 24–26, Jan. 2002.

[20] T. Dogaru, L. Collins, and L. Carin, "Optimal time-domain detection of a deterministic target buried under a randomly rough interface," *IEEE Trans. Antennas Propagat.*, vol. 49, pp. 313–326, Mar. 2001.

[21] J. T. Johnson and R. J. Burkholder, "Coupled canonical grid/discrete dipole approach for computing scattering from objects above or below a rough interface," *IEEE Trans. Geosci. Remote Sensing*, vol. 39, pp. 1214–1220, June 2001.

[22] K. O'Neill, "Broadband bistatic coherent and incoherent detection of buried objects beneath randomly rough surfaces," *IEEE Trans. Geosci. Remote Sensing*, vol. 38, pp. 891–898, Mar. 2000.

[23] G. Zhang, L. Tsang, and K. Pak, "Angular correlation function and scattering coefficient of electromagnetic waves scattered by a buried object under a two-dimensional rough surface," *J. Opt. Soc. Amer. A*, vol. 15, no. 12, pp. 2995–3002, Dec. 1998.

[24] J. R. Arias-Gonzalez, M. Nieto-Vesperinas, and A. Madrazo, "Morphology-dependent resonances in the scattering of electromagnetic waves from an object buried beneath a plane or a random rough surface," *J. Opt. Soc. Amer. A*, vol. 16, no. 12, pp. 2928–2934, Dec. 1999.

[25] R. R. Marchand and G. Brown, "Inferring rough surface parameters from average scattering data approximate scattering models; 1. Gaussain spectrum," *Radio Sci.*, vol. 33, no. 4, pp. 821–834, July–Aug. 1998.
[26] ——, "Inferring rough surface parameters from average scattering data approximate scattering models; 2. Pierson–Moskowitz spectrum," *Radio Sci.*, vol. 33, no. 4, pp. 835–843, July–Aug. 1998.
[27] V. Malyshkin, S. Simeonov, A. R. McGurn, and A. A. Maradudin, "Determination of surface profile statistics from electromagnetic scattering data," *Opt. Lett.*, vol. 22, no. 1, pp. 58–60, Jan. 1997.
[28] J. C. Stover, S. A. Serati, and C. H. Gillespie, "Calculation of surface statistics from light scatter," *Opt. Eng.*, vol. 23, no. 4, pp. 406–412, July/Aug. 1984.
[29] R. J. Wombel and J. A. DeSanto, "The reconstruction of shallow rough-surface profiles from scattered field data," *Inv. Prob.*, vol. 7, pp. 7–12, 1991.
[30] R. J. Wombell and J. A. DeSanto, "Reconstruction of rough-surface profiles with the Kirchhoff approximation," *J. Opt. Soc. Amer. A*, vol. 8, no. 12, pp. 1892–1897, 1991.
[31] J. C. Quartel and C. J. R. Sheppard, "A surface reconstruction algorithm based on confocal interferometric profiling," *J. Modern Opt.*, vol. 43, no. 3, pp. 591–605, 1996.
[32] ——, "Surface reconstruction using an algorithm based on confocal imaging," *J. Modern Opt.*, vol. 43, no. 3, pp. 469–468, 1996.
[33] D. Macias, E. R. Mendez, and V. Ruiz-Cortes, "Inverse scattering with a wave-front-matching algorithm," *J. Opt. Soc. Amer. A*, vol. 19, no. 10, Oct. 2002.
[34] V. Galdi, D. A. Castanon, and L. B. Felsen, "Multifrequency reconstruction of moderately rough interfaces via quasiray Gaussian beams," *IEEE Trans. Geosci. Remote Sensing*, vol. 40, pp. 453–460, Feb. 2002.
[35] V. Galdi, J. Pavlovich, W. C. Karl, D. A. Castanon, and L. B. Felsen, "Moderately rough dielectric interface profile reconstruction via short-pulse quasi-ray Gaussian beams," *IEEE Trans. Antenna Propagat.*, vol. 51, pp. 672–677, Mar. 2003.
[36] V. Galdi, H. Feng, D. A. Castanon, W. C. Karl, and L. B. Felsen, "Moderately rough surface underground imaging via short-pulse quasi-ray Gaussian beams," *IEEE Trans. Antenna Propagat.*, vol. 51, pp. 2304–2318, Sept. 2003.
[37] ——, "Multifrequency subsurface sensing in the presence of a moderately rough air-soil interface via quasiray Gaussian beams," *Radio Sci.*, vol. 38, no. 2, p. 8007, 2003.
[38] K. Harada and A. Noguchi, "Reconstruction of two-dimensional rough surface with Gaussian beam illumination," *IEICE Trans. Electron.*, vol. E79, no. 10, pp. 1345–49, 1996.
[39] V. Rokhlin, "Rapid solution of integral equations of scattering theory in two dimensions," *J. Comput. Phys.*, vol. 36, pp. 414–439, 1990.
[40] C. C. Lu and W. C. Chew, "A multilevel fast-algorithm for solving a boundary integral equation of wave scattering," *Microwave Opt. Technol. Lett.*, vol. 7, pp. 466–470, July 1994.
[41] V. Jandhyala, "Fast multilevel algorithms for the efficient electromagnetic analysis of quasi-planar structures," Ph.D. thesis, Dept. Elect. Comput. Eng., Univ. Illinois, Urbana-Champaign, 1998.
[42] L. Medgyesi-Mitschang, J. Putnam, and M. Gedera, "Generalized method of moments for three-dimensional penetrable scatterers," *J. Opt. Soc. Amer. A*, vol. 11, no. 4, pp. 1383–1398, Oct. 1994.
[43] S. Rao, D. Wilton, and A. Glisson, "Electromagnetic scattering by surfaces of arbitrary shape," *IEEE Trans. Antennas Propagat.*, vol. AP-30, pp. 409–418, May 1982.
[44] R. Fletcher and M. J. D. Powell, "A rapid descent method for minimization," *Comput. J.*, vol. 6, pp. 163–168, 1963.
[45] R. Fletcher, "A new approach to variable metric algorithms," *Comput. J.*, vol. 13, no. 3, pp. 317–322, Aug. 1970.
[46] ——, *Practical Methods of Optimization*. New York: Wiley, 1981, vol. 2.
[47] F. Natterer and F. Wubbeling, *Mathematical Methods in Image Reconstruction*. Philadelphia, PA: SIAM, 2001.
[48] O. Dorn, E. Miller, and C. Rappaport, "A shape reconstruction method for electromagnetic tomography using adjoint fields and level sets," *Inv. Prob.*, vol. 16, pp. 1119–1156, 2000.
[49] M. N. O. Sadiku, *Numerical Techniques in Electromagnetics*, 2nd ed. Boca Raton, FL: CRC, 2001.
[50] L. L. Schumaker, *Spline Functions Basic Theory*. New York: Wiley, 1981.
[51] C. de Boor, *Applied Mathematics Sciences*. New York: Springer-Verlag, 1978, vol. 27, A Practical Guide to Splines.
[52] M. El-Shenawee, "Remote sensing of objects buried beneath 2-D random rough surfaces using the modified Mueller matrix elements," *J. Opt. Soc. Amer.*, vol. 20, pp. 183–194, Jan. 2003.

Magda El-Shenawee (M'91–SM'02) received the B.S. and M.S. degrees from Assiut University, Assiut, Egypt, and the Ph.D. degree from the University of Nebraska, Lincoln, in 1991, all in electrical engineering.

In 1992, she was a Research Associate in the Center for Electro-Optics, University of Nebraska, where she focused on the problem of enhanced backscatter phenomena. In 1994, she was a Research Associate with the National Research Center, Cairo, Egypt, and in 1997, she was a Visiting Scholar with the University of Illinois at Urbana-Champaign. In 1999, she joined the Multidisciplinary University Research Initiative (MURI) at Northeastern University, Boston, MA. She is currently an Associate Professor in the Department of Electrical Engineering, University of Arkansas, Fayetteville. Her research areas are rough surface scattering, computational electromagnetics, subsurface sensing of buried objects, breast cancer modeling, microwave imaging systems, inverse scattering, and numerical methods for microstrip circuits.

Dr. El-Shenawee is a member of the Eta Kappa Nu electrical engineering honor society.

Eric L. Miller (S'90–M'95-SM'03) received the S.B., S.M., and Ph.D. degrees from the Massachusetts Institute of Technology, Cambridge, in 1990, 1992, and 1994, respectively, all in electrical engineering and computer science.

He is currently an Associate Professor in the Department of Electrical and Computer Engineering, Northeastern University, Boston, MA. His research interests include physics-based tomographic image formation and object characterization, inverse problems in general and inverse scattering in particular, regularization, statistical signal and imaging processing, and computational physical modeling. This work has been carried out in the context of applications including medical imaging, nondestructive evaluation, environmental monitoring and remediation, landmine and unexploded ordnance remediation, and automatic target detection and classification.

Dr. Miller is a member of Tau Beta Pi, Eta Kappa Nu, and Phi Beta Kappa. He was an Associate Editor for the IEEE TRANSACTIONS ON IMAGE PROCESSING from 1998 to 2002 and is currently an Associate Editor for the IEEE TRANSACTIONS ON GEOSCIENCE AND REMOTE SENSING. He received the CAREER Award from the National Science Foundation in 1996 and the Outstanding Research Award from the College of Engineering at Northeastern University in 2002.